
Article:
Hoang, K. orcid.org/0000-0001-7463-9681 (2020) Simplified analytical model for rapid evaluation of interior PM traction machines considering magnetic nonlinearity. IEEE Open Journal of the Industrial Electronics Society, 1. pp. 340-354. ISSN 2644-1284

https://doi.org/10.1109/OJIES.2020.3042950

Date of publication xxxx 00, 0000, date of current version xxxx 00, 0000.
Digital Object Identifier XX.XXXX/YYY.20XX.ZZZZZZZ

Simplified Analytical Model for Rapid Evaluation of Interior PM Traction Machines Considering Magnetic Nonlinearity

Khoa Dang Hoang, (Senior Member, IEEE)
Electrical Machines and Drives Group, Department of Electronic and Electrical Engineering, University of Sheffield, Mappin Building, Mappin Street, S1 3JD, Sheffield, United Kingdom.

Corresponding author: Khoa Dang Hoang (e-mail: k.hoang@sheffield.ac.uk).

ABSTRACT The article presents an analytically rapid evaluation technique for interior permanent magnet (IPM) traction machines considering magnetic nonlinearity. First, a simplified model employing equivalent magnetic circuit together with winding function to determine no-load airgap flux density and *dq*-axis armature-reaction airgap flux densities for parameter determination is proposed. Then, a process loop is utilized for nonlinear magnetic analysis under full range on-load *dq*-axis currents. Using the obtained parameter information, losses/efficiency determination for tested machine could be achieved. It is shown that in the field-weakening (FW) operation region, the high-order synchronous flux density harmonics highly contributing to machine iron loss may also significantly contribute to magnetic saturation and therefore should be considered together with fundamental component for nonlinear magnetic analysis. In comparison to computationally expensive finite element analysis (FEA), sufficiently accurate parameters and efficiency for tested machine could be obtained within minutes. Thus, the proposed technique is very essential to rapidly evaluate a given design specification at the preliminary design stage where repeated adjustment on design specification is necessary for a multi-physics optimization achievement and with that, repeated re-construction and re-evaluation of FEA model may be undesirable. The proposed method is validated by FEA for a high-speed high-power (15krpm/120kW) IPM traction machine.

INDEX TERMS Efficiency determination, IPM machine, magnetic nonlinearity, parameter determination.

I. INTRODUCTION

Due to their high efficiencies and good field weakening capabilities, interior permanent magnet (IPM) machines are often designed for traction applications [1], [2]. However, IPM machines are well-known for their highly nonlinear characteristics and therefore, computationally expensive finite element analysis (FEA) is often employed for evaluating a given design specification (i.e. parameter and efficiency determination). Obviously, at the preliminary design stage where repeated adjustment on design specification is necessary for a multi-physics optimization achievement and with that, repeated re-construction together with re-evaluation of the highly time-consuming FEA model may be undesirable, a reasonably accurate and fast technique for rapidly evaluating an IPM machine design specification without requirement of the highly time-consuming FEA is highly essential.

Analytical researches for IPM machine were presented in [3]-[17]. Air-gap field analysis of a line-start IPM machine for determination of *dq*-axis inductances and back-EMF was introduced in [3]. Synchronous reactance calculation for different PM synchronous machines was proposed in [4]. Compromised effect due to the outer-bridge on IPM machine air-gap flux density was reported in [5]. In [6] and [7], high fidelity equivalent magnetic circuit (EMC) models of IPM machine using network theory considering each stator iron slot segment, iron yoke segment, and main rotor iron region as a network element were proposed. To achieve an equilibrium operation point considering magnetic nonlinearity, multi-loop-variables represented for the network elements must be iterated within a process loop until a desired error level could be satisfied. However, only *d*-axis inductance as a function of *d*-axis current and *q*-axis inductance as a function of *q*-axis current were presented. In [8], EMC model was employed to predict IPM machine open-circuit airgap field distribution. On the other hand, winding function was utilized in [9]-[11] to calculate IPM machine armature-reaction airgap flux density. However, only *dq*-axis armature-reaction airgap flux densities for a given set of *dq*-axis currents were presented. It is noted that

the winding function technique was proven to be suitable for analyzing both IPM machines with distributed-winding configuration and fractional-slot concentrated-winding (FSCW) configuration, [10]. In [12], a simplified EMC model with an equivalent single conductor representing the whole machine winding for IPM machine inductance calculation was introduced. However, only no-load *dq*-axis inductances were presented. In [13], a high fidelity EMC model with 10 layers (1 to 72 nodes per layer) was introduced for computing the PM working points of an IPM machine under no-load and rated-load conditions. Combination of EMC model and exact conformal mapping technique for calculating IPM machine open-circuit airgap field distribution was proposed in [14]. Analytical models for IPM machine considering slot effect and cogging torque was introduced in [15] and [16]. However, only analysis result as a function of phase current (*q*-axis) was presented in [15] and analysis result of one specific operation point was shown in [16]. In [17], a high fidelity EMC model considering individual stator slot reluctances, segmented airgap reluctances, and segmented rotor reluctances was suggested. However, two separate nested-process-loops with multi-loop-variables must be solved for determining one operation point. As a result, computation time of the proposed method in [17] is only reduced by 30% compared with the FEA. To the best knowledge of the author, analytically rapid solution for sufficiently predicting IPM machine parameters from a given design specification considering magnetic nonlinearity under full range on-load *dq*-axis currents is quite limited and this is the main subject of the paper.

For rapid efficiency determination of IPM machine, prediction of electromagnetic losses over torque-speed performance is essentially required. Analytical equations for IPM machine copper AC loss and windage losses were presented in [18]. In [19]-[21], IPM machine iron loss in deep FW operation which are mainly contributed by high-order synchronous harmonic eddy-current loss was presented. Empirical validation of IPM machine copper and iron losses considering harmonic effects was introduced in [22]. Obviously, reliable electromagnetic loss estimation highly depends on accurate information of machine parameters.

The main target of the paper is to develop a reasonably accurate and fast analytical evaluation technique for rapid parameter and efficiency determination of IPM traction machines considering magnetic nonlinearity under full range on-load *dq*-axis currents. The proposed technique achieves the objective for the studied IPM by 3 steps:

1. Developing a simplified analytical model for determining *dq*-axis airgap flux densities from a given IPM machine design specification using EMC model (for determining the open-circuit airgap flux density) together with winding function (for determining the *dq*-axis armature-reaction airgap flux densities). The obtained fundamental components are used to calculate machine parameters. Under the proposed model, the average magnetomotive force (MMF) drops on the *dq*-axis iron-cores are represented by the relevant *dq*-axis equivalent airgap lengths defined from the simplified EMC model. Thus, only a single loop-variable must be iterated within a process loop for nonlinear magnetic analysis of one operation point (see Fig. 7).
2. Demonstrating the effects of the synchronous flux density harmonics on machine magnetic saturation under high-*d*-axis current and low-*q*-axis current (FW) operation region.
3. Iterating the proposed simplified model considering synchronous flux density harmonics for nonlinear magnetic analysis over the full range on-load *dq*-axis currents to obtain the relevant machine parameter information. The obtained parameters are used to determine optimum *dq*-axis currents over torque-speed performance map and the relevant copper loss whereas the obtained synchronous flux densities are used to determine the relevant iron loss. The obtained loss information is employed to define machine efficiency. It is noted that determination of optimum *dq*-axis currents over torque-speed performance map was well presented in [1], [2] and [23] and is not discussed in the paper to avoid duplication.

In comparison with high fidelity EMC model techniques [6], [7], [13], [17] where multi-loop-variables must be iterated within a process loop, the proposed method with only a single loop-variable is simpler and therefore could be employed for rapid nonlinear magnetic analysis under full range on-load *dq*-axis currents with a reasonably accurate level. Under the proposed method, sufficiently accurate machine parameters (up to 10% difference under extreme-saturation and deep-FW operations), and efficiency (up to 1% efficiency difference within main torque-speed operation region) of the tested IPM machine compared with FEA can be produced within minutes. Thus, the proposed technique is very essential to quickly evaluate a defined IPM machine design specification at the preliminary design stage where repeated adjustment of design specification is necessary for a multi-physics optimization achievement and with that, repeated re-construction together with re-evaluation of the FEA model may be undesirable. The proposed method is validated by FEA for a high-speed high-power IPM traction machine.

The remaining parts of the paper is organized as follows. The simplified EMC model for the proposed technique is described in Section II. Combination of EMC model and winding function to determine *dq*-axis airgap flux densities as well as parameters is introduced in Section III. Section IV demonstrates the necessary of considering the synchronous airgap flux density harmonics together with the fundamental component for nonlinear magnetic analysis. Loss determination for the studied IPM machine is discussed in Section V. Section VI provides analysis results from the proposed technique compared with resultant FEA acting as a benchmark. Some conclusions are discussed in Section VII.

TABLE 1. Principal Design Specification of Tested IPM Machine [18]

Symbol	Design specification	Value
B_{mr}	PM remanence (T)	1.217
D_{is}	Stator inner diameter (mm)	93.716
D_{os}	Stator outer diameter (mm)	155
d_{stnd}	Strand diameter	AWG21
l_g	Airgap length (mm)	0.728
l_{ib}	Rotor inner-bridge length (mm)	0.8
l_m	Magnet length (mm)	5
l_{ob}	Rotor outer-bridge length (mm)	0.8
l_{stk}	Stator stack length (mm)	160
n_p	Number of pole pair	4
n_{slt}	Number of slot	48
n_{stnd}	Number of strands per conductor	20
n_t	Number of turn	32
s_{dpt}	Stator slot depth (mm)	19.5
s_{op}	Stator slot opening (mm)	1.73
s_{wg}	Stator slot wedge (mm)	0.543
t_{dpt}	Slot tang depth (mm)	1
t_{wd}	Stator tooth width (mm)	3.72
w_m	Magnet width (mm)	27
y_{wd}	Stator yoke width (mm)	11.11
α_{br}	Flux barrier angle (elect. degree)	45.65
α_{lm}	Flux barrier width angle (elect. degree)	17.4
α_{pa}	Pole-arc angle (elect. degree)	133.5

TABLE 2. Specifications of Tested IPM Machine [18]

Continuous / Peak torque (Nm)	112.5 / 225
Peak current (A) / DC-link voltage (V)	310 / 600
Base / Maximum speed (rpm)	5850 / 15000
Number of pole pair	4

II. SIMPLIFIED EQUIVALENT MAGNETIC CIRCUIT FOR RAPID EVALUATION OF IPM MACHINES

In [24], a sizing concept for IPM traction machine was proposed. By using the concept, a high-speed high-power (15krpm, 120kW) IPM traction machine has been designed and manufactured [18] as shown in Fig. 1 and the principal design specification together with symbol definitions are presented in Tables 1 and 2 (some tooth dimensions are defined in section III.D). The tested machine is equipped with single-layer distributed winding with a high current density (30.36A/mm^2 with $I_{\max}$ = 310A) at the short-period overload peak torque as 225Nm associated with a peak fundamental airgap flux density as 1.25T and a relevant high-saturated tooth flux density as 2.04T [18].

A. SIMPLIFIED EQUIVALENT MAGNETIC CIRCUIT FOR PROPOSED TECHNIQUE

In Fig. 1(a), assuming both the rotor outer-bridge and inner-bridge are always saturated with a similar flux density level B_{sat}, an equivalent rotor outer-bridge of which equivalent length is as $l_{brd} = l_{ob} + l_{ib}$ represented for both the rotor outer- and inner-bridge could be defined with $A_{bdg} = l_{bdg}l_{stk}$ is the equivalent rotor outer-bridge area. Using the equivalent rotor outer-bridge, according to [24], the machine geometry in Fig. 1(a) could be represented by a simplified EMC model for one-half machine pole pair as

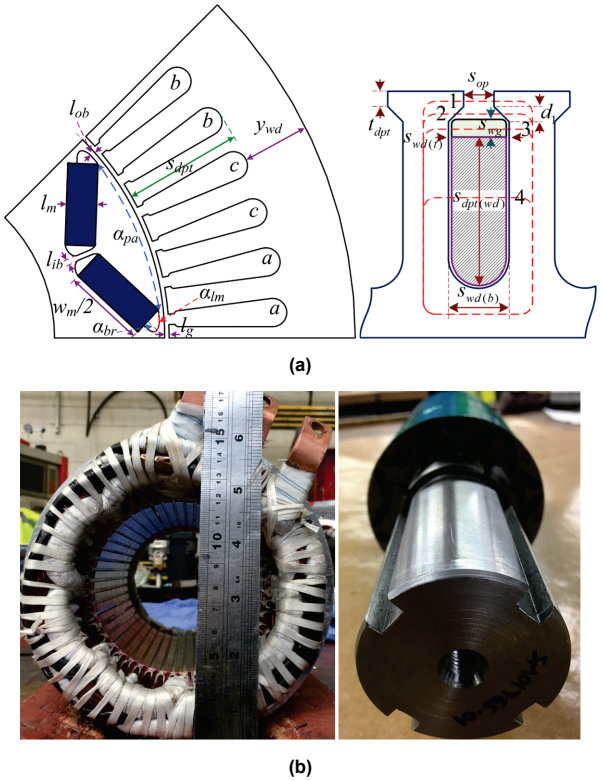

FIG. 1. Studied IPM traction machine [18]. (a) Geometries [see Table 1 for symbol definitions, some tooth dimensions are defined in section III.D]. (b) Machine prototype.

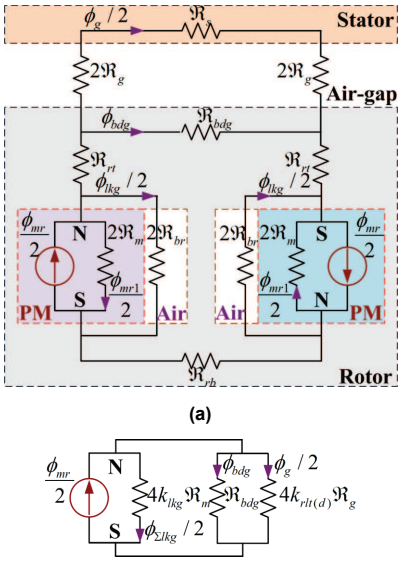

FIG. 2. EMC model for one-half machine pole pair [24], [25]. (a) Simplified EMC model. (b) Further simplified EMC model.

shown in Fig. 2(a) where $\Re_s$, $\Re_g$, $\Re_{bdg}$, $\Re_{rt}$, $\Re_{br}$, $\Re_m$, and $\Re_{rb}$ are respectively the stator reluctance, the airgap reluctance in the pole-arc range, the equivalent rotor outer-bridge reluctance, the rotor section on top PM reluctance, the rotor flux barrier reluctance, the PM reluctance, and the rotor section at bottom PM reluctance; ϕ_g, ϕ_{bdg}, ϕ_{lkg}, ϕ_{mr}, and ϕ_{mr1} are respectively the airgap flux, the rotor leakage flux

passing through the equivalent rotor outer-bridge, the PM leakage flux passing through the flux barrier, the PM main flux, and the PM leakage flux passing through the PM. It is noted that the stator slot effects are neglected in the proposed simplified analytical model (i.e. assuming a smooth stator), [8]-[11]. It is also noted that the tested IPM traction machine is a single-layer rotor geometry and EMC model for IPM machine with multilayer-type rotor geometry could be found in [6]-[8].

B. DETERMINATION OF DQ-AXIS EQUIVALENT AIRGAP LENGTH CONSIDERING MAGNETIC NONLINEARITY [24], [25]

For the simplified EMC model in Fig. 2(a), the effects of magnetic nonlinearity could be defined as a scaling reluctant factor $k_{rlt(d,q)}$ introduced in the airgap length l_g and represented for the average magnetomotive force (MMF) drop in the machine *dq*-axis iron-core [24], [25]. Due to its saturated characteristic resulting in its limited passing flux, effects of the $\Re_{bdg}$ on the machine average MMF drop could be neglected. Thus, an equivalent *dq*-axis iron-core reluctances $\Re_{Fe(d,q)}$ represented for the average MMF drop in one-half machine pole pair could be defined in (1) where $l_{Fe(d)} = [2s_{dpt}+y_{wd}+(4/6)\pi(2D_{is}+s_{dpt}-2l_g)/(2n_p)-2l_m]$ is the relevant *d*-axis average iron-core length, $A_{Fe} = n_{slt}t_{wd}l_{stk}/(2n_p)$ is the iron-core area over one pole-pitch. Since the *q*-axis flux lines do not cross the PM [see Fig. 3(b)], the relevant *q*-axis average iron-core length, $l_{Fe(q)}$, is higher than $l_{Fe(d)}$ a value as $2l_m$. It is noted that the factor (4/6) in the $l_{Fe(d)}$ is the average ratio based on the number of slots per pole (6 slot per pole) for the tested machine.

$$\Re_{Fe(d,q)} \approx \Re_s + 2\Re_{rt} + \Re_{rb} = 2l_{Fe(d,q)} / (\mu_0\mu_{rFe}A_{Fe}) \quad (1)$$

On the other hand, the airgap reluctance in the pole-arc range is $\Re_g = l_g k_{Ca} / (\mu_0 A_g)$ with $A_g = \alpha_{pa}D_{is}l_{stk}/(2n_p)$ is the airgap area in the pole-arc range and k_{Ca} is the Cater factor [25], [26]. Based on the EMC model in Fig. 2(a), relevant scaling reluctant factors, $k_{rlt(d,q)}$, represented for the average MMF drops on the *dq*-axis iron-cores over the airgap length could be expressed in (2).

$$\begin{aligned} k_{rlt(d,q)} &= (\Re_{Fe(d,q)} + 4\Re_g) / (4\Re_g) \\ &= 1 + (l_{Fe(d,q)}D_{is}\alpha_{pa} / 2\mu_{rFe}l_g k_{Ca}n_{slt}t_{wd}) \end{aligned} \quad (2)$$

Result from (2) could be used to determine the *dq*-axis equivalent airgap length $l^{eq}_{g(d)}$ and $l^{eq}_{g(q)}$ as a function of the relative permeability, μ_{rFe}, considering the average MMF drops on the relevant *dq*-axis iron-cores as shown in (3).

$$l^{eq}_{g(d,q)} = l_g k_{rlt(d,q)} k_{Ca} \quad (3)$$

III. PARAMETER DETERMINATION OF IPM MACHINES

A. DETERMINATION OF NO-LOAD AIRGAP FLUX DENSITY B_{gm} AND PM FLUX LINKAGE Ψ_m

By using (3), the EMC model in Fig. 2(a) is further simplified into Fig. 2(b) where k_{lkg} is represented for the PM leakage flux passing through the flux barrier which is very close to, but less than 1 [25]; $\phi_{\Sigma lkg} = \phi_{lkg} + \phi_{mr1}$ is the total PM leakage flux; $\phi_{mr} = B_{mr}A_m = B_{mr}l_m / (\mu_0\mu_{mr}\Re_m)$; $\phi_g = B_{gm}A_g = B_{gm}l^{eq}_{g(d)} / (\mu_0 k_{rlt(d)}\Re_g)$; $A_m = w_m l_{stk}$ is the PM area; $\phi_{bdg} = B_{sat}A_{bdg} = B_{sat}l_{bdg}l_{stk}$. Based on Fig. 2(b), the relation between ϕ_g, ϕ_{bdg}, and ϕ_{mr}, is presented in (4) and (5).

$$\phi_g = \phi_{mr} / [1 + (k_{rlt(d)}\Re_g / k_{lkg}\Re_m) + (4k_{rlt(d)}\Re_g / \Re_{bdg})] \quad (4)$$

$$\phi_{bdg} = \phi_{mr} / [2 + (\Re_{bdg} / 2k_{rlt(d)}\Re_g) + (\Re_{bdg} / 2k_{lk}\Re_m)] \quad (5)$$

Rearranging (4) to obtain (6) for determining the airgap flux density from the rotor PM, B_{gm}, where $k_{A(M2G)}=w_m/[\alpha_{pa}D_{or}/(2n_p)]$ is the ratio between the magnet and the airgap area; $k_{\Re(B2G)}$ defined in (7) is the ratio between the equivalent outer-bridge reluctance and the airgap magnetic reluctance obtained by rearranging (5).

$$B_{gm} = \frac{B_{mr}k_{A(M2G)}}{[1 + (\mu_{rm}l^{eq}_{g(d)}k_{A(M2G)} / k_{lkg}l_m) + (4k_{rlt(d)} / k_{\Re(B2G)})]} \quad (6)$$

$$k_{\Re(B2G)} = \frac{(B_{mr} / B_{sat})(w_m / l_{bdg}) - 2}{(1 / 2k_{rlt(d)}) + (\mu_{rm}l_g k_{Ca}k_{A(M2G)}) / (2l_m k_{lkg})} \quad (7)$$

In practice, the no-load airgap flux density generated by the PM could be expressed as a piecewise function rotating synchronously with the rotor and aligning with *d*-axis as shown in (8) where θ is the electrical angular position in the stator reference frame measured from the axis of phase *a*; ωt is the instantaneous rotor angular position, v is the harmonic orders associated with the rotating rotor (v = 1,3,5…), [26]. Based on (8), the fundamental PM flux linkage could be obtained using (9) where $k_{B2\psi} = (k_{wd(1)}n_t D_{is}l_{stk}/n_p)$ is the flux density to flux linkage conversion ratio; $k_{wd(1)}$ is the fundamental winding factor [26].

$$B_{g\_PM}(\theta,t) = B_{gm}\frac{4}{\pi}\sum_v \frac{\sin(v\alpha_{pa}/2)}{v}\cos[v(\theta - \omega t)] \quad (8)$$

$$\psi_{m1} = k_{B2\psi}B_{g\_PM(1)} \quad (9)$$

B. DETERMINATION OF STATOR MMF AND DQ-AXIS ARMATURE-REACTION AIRGAP FLUX DENSITIES

1) DETERMINATION OF STATOR MMF

In general, the synthetic MMF, $F_{s\Sigma}(\theta,t)$, generating by the three phase symmetric currents and winding function [9]-[11], [26] could be obtained in (10) where $F_{s(h)} = (3/2)[(4/\pi)k_{wd(h)}n_t/(h2n_p)]I_{m1}$ is the amplitude of the *h*-order harmonic (h = 1,5,7,11…); $k_{wd(h)}$ is the relevant winding factor; I_{m1} is the current magnitude; φ is the phase current angle measured from the *d*-axis; k_h = -1 for $h = 6(m-1)+1$; k_h = 1 for $h = 6m-1$; (m = 1,2,3…). The relevant *dq*-axis MMF components, $F_{s(d)\Sigma}(\theta,t)$ and $F_{s(d)\Sigma}(\theta,t)$, are shown in (11) [10], [11], [26].

$$\begin{aligned} F_{s\Sigma}(\theta,t) &= \sum_h F_{s(h)}\cos[(h\theta + k_h\omega t) - \varphi] \\ &= F_{s(d)\Sigma}(\theta,t) + F_{s(q)\Sigma}(\theta,t) \end{aligned} \quad (10)$$

$$F_{s(d)\Sigma}(\theta,t) = \sum_h F_{s(h)}\cos(h\theta + k_h\omega t)\cos(\varphi) \quad (11.a)$$

$$F_{s(q)\Sigma}(\theta,t)=\sum_h F_{s(h)}\sin(h\theta+k_h\omega t)\sin(\varphi) \qquad (11.b)$$

In the ideal case without the rotor armature-reaction, the ideal *dq*-axis armature-reaction airgap flux densities, $B_{g(d,q)\_armID}(\theta,t)$, could be defined as (12) [9], [26], [27].

$$B_{g(d,q)\_armID}(\theta,t)=(\mu_0/l^{eq}_{g(d,q)})F_{s(d,q)\Sigma}(\theta,t) \qquad (12)$$

In practice, due to the rotor barriers resulting in the rotor armature-reaction, the *dq*-axis armature-reaction airgap MMFs, $F_{g(d,q)\_arm}(\theta,t)$, considering the *dq*-axis rotor MMFs, $F_{r(d,q)\_arm}(\theta,t)$, could be expressed in (13) assuming the positive direction of the reference system is from rotor to stator [9]-[11], [27]. The result from (13) could be used to compute the *dq*-axis armature-reaction airgap flux densities, $B_{g(d,q)\_arm}(\theta,t)$, (14).

$$F_{g(d,q)\_arm}(\theta,t)=F_{s(d,q)\Sigma}(\theta,t)-F_{r(d,q)\_arm}(\theta,t) \qquad (13)$$

$$B_{g(d,q)\_arm}(\theta,t)=(\mu_0/l^{eq}_{g(d,q)})F_{g(d,q)\_arm}(\theta,t) \qquad (14)$$

2) DETERMINATION OF *D*-AXIS ARMATURE-REACTION AIRGAP FLUX DENSITY

Magnetic flux diagrams with the rotor located at the *d*- and *q*-axis is respectively represented in Fig. 3(a) and 3(b) where a single conductor is employed to represent the whole machine stator winding [12]. In Fig. 3(a), for simplicity, both the flux lines passing through the outer/inner rotor bridges and the flux barrier could be neglected and the flux lines entering the pole-cap could be assumed to be equal to the flux lines passing out through the PM. On the other hand, since the upper and lower surface of the PM is surrounded by magnetic material, the magnetic potential of the PM could be considered to be constant referring to rotor position and therefore could be modeled as only a function of time. Thus, the relevant rotor magnetic potential waveform induced by the stator MMF could be expressed as a piecewise function rotating synchronously with the rotor and aligning with *d*-axis as shown in Fig. 4(a) and described in (15) where U_{d_arm} is the magnitude of the magnetic potential, [9]-[11]; ν is the harmonic orders associated with the rotating rotor (ν = 1,3,5…).

$$F_{r(d)\_arm}(\theta,t)=U_{d\_arm}\frac{4}{\pi}\sum_{\nu}\frac{\sin(\nu\alpha_{pa}/2)}{\nu}\cos[\nu(\theta-\omega t)] \qquad (15)$$

Based on the continuity theory of the magnetic flux, the U_{d_arm} for the range ($-0.5\alpha_{pa}$, $0.5\alpha_{pa}$) could be derived via (16) where r is the airgap radius, $(D_{or}/2) \le r \le (D_{is}/2)$ [9]-[11], [27]. For simplicity, r is selected as $D_{is}/2$ in the paper.

$$\begin{aligned}U_{d\_arm}&=\frac{\Re_m}{n_p}\int_{-0.5\alpha_{pa}+\omega t}^{0.5\alpha_{pa}+\omega t}B_{g(d)\_arm}(\theta,t)rl_{stk}d\theta\\&=\frac{\Re_m}{\Re_m+\Re_g}\sum_h\frac{F_{s(h)}}{h}\frac{\sin(h\alpha_{pa}/2)}{\alpha_{pa}/2}\cos[(h+k_h)\omega t]\cos(\varphi)\end{aligned} \qquad (16)$$

Substituting (15) and (16) into (14) to obtain (17) for determining the *d*-axis armature-reaction airgap flux density.

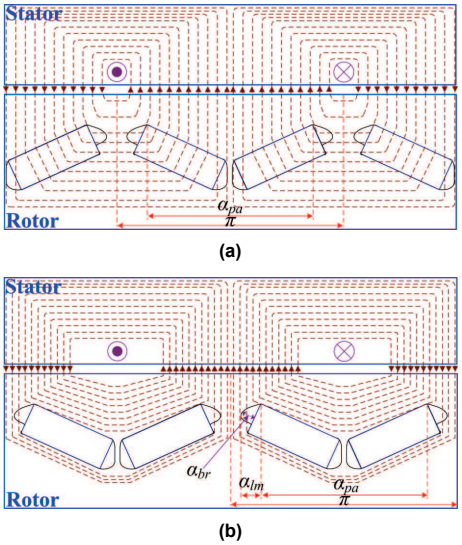

FIG. 3. Armature-reaction flux lines [12]. (a) Rotor is located at the *d*-axis. (b) Rotor is located at the *q*-axis.

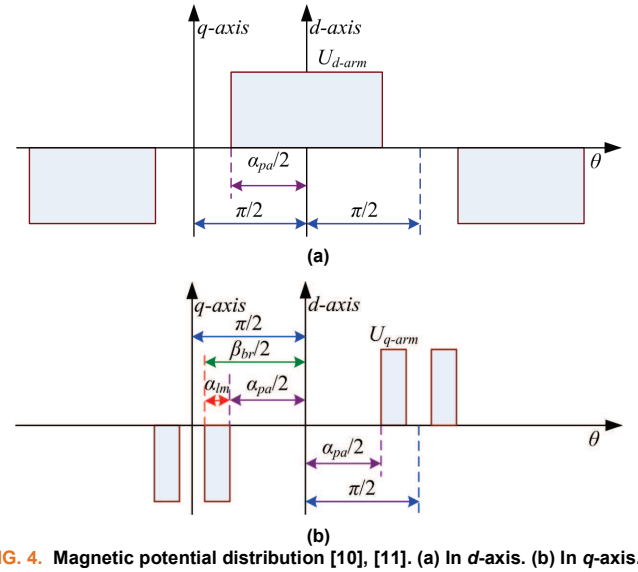

FIG. 4. Magnetic potential distribution [10], [11]. (a) In *d*-axis. (b) In *q*-axis.

$$\begin{aligned}B_{g(d)\_arm}(\theta,t)=&(\mu_0/l^{eq}_{q(d)})\cos(\varphi)[\sum_h F_{s(h)}\cos(h\theta+k_h\omega t)\\&-\frac{\Re_m}{\Re_m+\Re_g}\sum_h\frac{F_{s(h)}}{h}\frac{\sin(h\alpha_{pa}/2)}{\alpha_{pa}/2}\cos[(h+k_h)\omega t]\\&\times\frac{4}{\pi}\sum_{\nu}\frac{\sin(\nu\alpha_{pa}/2)}{\nu}\cos[\nu(\theta-\omega t)]]\end{aligned} \qquad (17)$$

3) DETERMINATION OF *Q*-AXIS ARMATURE-REACTION AIRGAP FLUX DENSITY

The *q*-axis armature-reaction flux lines passing through the flux barriers in Fig. 3(b) also result in a relevant rotor magnetic potential [10], [11]. For simplicity, its value could be considered as constant referring to rotor position and therefore could be modeled only as a function of time [10], [11]. Thus, the relevant rotor magnetic potential waveform induced by the stator MMF could be expressed as a piecewise function rotating synchronously with the rotor and aligning with *d*-axis as shown in Fig. 4(b) and

described in (18) where U_{q_arm} is the magnitude of the magnetic potential; α_{lm} is flux barrier width angle defined as a half of the different angle between the barrier-arc angle, β_{br}, and the pole-arc angle, α_{pa}, [10], [11] [see Figs. 3(b) and 4(b)]; v is the harmonic orders associated with the rotating rotor (v = 1,3,5…).

$$F_{r(q)\_arm}(\theta,t) = U_{q\_arm}\frac{4}{\pi} \times\sum_{v}\frac{\cos(v\alpha_{pa}/2)-\cos[v(\alpha_{pa}/2)+v\alpha_{lm}]}{v}\sin[v(\theta-\omega t)] \quad (18)$$

Based on the continuity theory of the magnetic flux, the U_{q_arm} for the range ($0.5\alpha_{pa}$, $0.5\alpha_{pa}+\alpha_{lm}$) could be obtained via (19) where $\mathrm{P}_{br} = 1/[(1/\mathrm{P}_{gbr(lm)})-(1/\mathrm{P}_{g(lm)})]$ is the flux barrier permeance; $\mathrm{P}_{g(lm)} = \mu_0 D_{is}\alpha_{lm} l_{stk}/(l_{g(q)}^{eq} 2n_p)$ is the relevant airgap permeance; $\mathrm{P}_{gbr(lm)} = (\mu_0 l_{stk}/\alpha_{br} n_p)\ln[[(D_{is}/2)\alpha_{lm}\alpha_{br}/l_{g(q)}^{eq}]+1]$ is the relevant equivalent permeance for both airgap and flux barrier [10], [11].

$$U_{q\_arm} = \frac{1}{n_p \mathrm{P}_{br}}\int_{0.5\alpha_{pa}+\omega t}^{0.5\alpha_{pa}+\alpha_{lm}+\omega t} B_{g(q)\_arm}(\theta,t) r l_{stk} d\theta = \frac{2\mu_0 r l_{stk}}{n_p l_{g(q)}^{eq}(\mathrm{P}_{br}+\mathrm{P}_{g(lm)})} \times\sum_{h}\frac{F_{s(h)}}{h}\sin(h\frac{\alpha_{lm}}{2})\sin[h\frac{\alpha_{pa}+\alpha_{lm}}{2}+(h+k_h)\omega t]\sin(\varphi) \quad (19)$$

Substituting (18) and (19) into (14) to obtain (20) for determining the q-axis armature-reaction airgap flux density.

$$B_{g(q)\_arm}(\theta,t) = (\mu_0/l_{g(q)}^{eq})\sin(\varphi)[\sum_h F_{s(h)}\sin(h\theta+k_h\omega t) - \frac{2\mu_0 r l_{stk}}{n_p l_{g(q)}^{eq}(\mathrm{P}_{br}+\mathrm{P}_{g(lm)})} \times\sum_h\frac{F_{s(h)}}{h}\sin(h\frac{\alpha_{lm}}{2})\sin[h\frac{\alpha_{pa}+\alpha_{lm}}{2}+(h+k_h)\omega t] \times\frac{4}{\pi}\sum_v\frac{\cos(v\alpha_{pa}/2)-\cos[v(\alpha_{pa}/2)+v\alpha_{lm}]}{v}\sin[v(\theta-\omega t)]] \quad (20)$$

C. DETERMINATION OF DQ-AXIS INDUCTANCES

Based on the obtained dq-axis airgap flux densities in (17) and (20), the dq-axis inductance of IPM machine is determined as shown in (21) where $k_{ad(dq)}$ is the dq-axis adjustment factors associated with the difference in the fundamental value between the actual dq-axis armature-reaction airgap flux densities (17), (20) and the ideal case (12) [4], [26], [27]; L_{lk} is the phase leakage inductance.

$$L_{d,q} = L_{lk} + k_{ad(d,q)}(3/\pi)(k_{wd(1)}n_t/n_p)^2\mu_0 D_{is} l_{stk}/l_{g(d,q)}^{eq} \quad (21)$$

where $k_{ad(d)} = 1-\frac{(4/\pi)\sin^2(\alpha_{pa}/2)}{[1+(\Re_g/\Re_m)](\alpha_{pa}/2)}$;

$$k_{ad(q)} = 1-\frac{2\mu_0 r l_{stk}}{n_p l_{g(q)}^{eq}}\frac{\sin[(\alpha_{pa}+\alpha_{lm})/2]\sin(\alpha_{lm}/2)}{(\mathrm{P}_{br}+\mathrm{P}_{g(lm)})} \times\frac{4}{\pi}[\cos(\alpha_{pa}/2)-\cos[(\alpha_{pa}/2)+\alpha_{lm}]]$$

D. DETERMINATION OF LEAKAGE INDUCTANCE

The leakage inductance L_{lk} includes the phase slot leakage inductance, L_{slk}, and the phase end-winding leakage inductance, L_{elk}, [26], [27]. The total slot leakage inductance associated with 4 main leakage path 1 to 4 (see Fig. 1a) considering magnetic nonlinearity is presented in (22). The end-winding leakage inductance L_{elk} is small and is not presented in the paper.

$$L_{slk} = \mu_o\frac{n_{slt}}{3}n_{tps}^2[\frac{t_{dpt}}{s_{op}k_{sat1}}+\frac{2d_1}{(s_{op}+s_{wd(t)})k_{sat2}} +\frac{s_{wg}}{s_{wd(t)}k_{sat3}}+\frac{2s_{dpt(wd)}}{3(s_{wd(t)}+s_{wd(b)})k_{sat4}}]l_{stk} \quad (22)$$

where $k_{sat1,2,3,4}$ is the scaling slot reluctant factors associated with relevant slot leakage flux path 1 to 4; $k_{sat1}=1+l_{slt1}/(\mu_{rFe}s_{op})$; $k_{sat2}=1+2l_{slt2}/\mu_{rFe}(s_{op}+s_{wd(t)})$; $k_{sat3}=1+l_{slt3}/(\mu_{rFe}s_{wd(t)})$; $k_{sat4}=1+2l_{slt4}/\mu_{rFe}(s_{wd(t)}+s_{wd(b)})$; $l_{slt1,2,3,4}$ is the relevant slot leakage flux path length on iron-core (easily obtained from the slot geometries and not presented in the paper); n_{tps} is the number of turn per slot per phase; $s_{dpt(wd)}$ is the slot depth of stator winding part; $s_{wd(t)}/s_{wd(b)}$ is the top-/bottom-slot width; d_1 is associated with the slot opening angle.

IV. PARAMETER DETERMINATION CONSIDERING MAGNETIC NONLINEARITY

A. EFFECTS OF SYNCHRONOUS HARMONICS ON MAGNETIC SATURATION OF IPM MACHINES

Based on the rotating speed, the dq-axis armature-reaction airgap flux density components in (17) and (20) could be categorized into two main parts. The first part is linked with the fundamental MMF component (h = 1) and its relevant associated v-order rotor MMF components (v = 1,3,5…) rotating synchronously with the rotor. The second part is linked with the high-order MMF components ($h \neq 1$) and their relevant associated v-order rotor MMF components (v = 1,3,5…) rotating asynchronously with the rotor. Therefore, the total airgap flux density of the tested IPM machine, $B_g(\theta,t)$, contributing by both the open-circuit airgap flux density rotating synchronously with the rotor (8) and the dq-axis armature-reaction flux densities, (17) and (20), could be rearranged into two separated components: $B_{gSyn}(\theta,t)$ (synchronously component) and $B_{gAsyn}(\theta,t)$ (asynchronously component), (23) and (24).

$$B_{gSyn}(\theta,t) = B_{g\_PM}(\theta,t)+B_{g(d)\_arm}(\theta,t)+B_{g(q)\_arm}(\theta,t) \quad \text{with } (h=1) \quad (23)$$

$$B_{gAsyn}(\theta,t) = B_{g(d)\_arm}(\theta,t) + B_{g(q)\_arm}(\theta,t) \quad \text{with } (h \neq 1) \tag{24}$$

In terms of harmonic magnitudes, the $F_{s(h)}$ element of the asynchronous armature-reaction h-order MMF component (h = 5,7,11…) and its relevant associated v-order rotor MMF components (v = 1,3,5…), (17) and (20), is respectively reduced by a factor as ($k_{wd(h)}/h$) [see (10)] and ($k_{wd(h)}/h^2$) [see (17) and (20)] compared with the synchronous fundamental component (h = 1). It is noted that IPM machines are well-known for their high synchronous v-order open-circuit airgap flux density harmonics (v = 1,3,5…), $B_{g\_PM}(\theta,t)$ [see (8)]. Since magnitudes of the asynchronous harmonics are significantly low compared with the synchronous harmonics, for simplicity, only the synchronous airgap flux density harmonics are considered for nonlinear magnetic analysis in the proposed technique (see Fig. 9). In the next section, it will show that the synchronous 3rd order harmonic highly contributes to magnetic saturation under high-d-axis current and low-q-axis current operation (see Fig. 5). It is also noted that the high-order synchronous flux density harmonics in (23) are essential for iron loss determination [20], [21].

Substituting (9) and (21) into (23) and rearranging to obtain the relation between machine parameters, machine design specification in Table I, and dq-axis v-order synchronous airgap flux density harmonics (v = 1,3,5…), (25) and (26).

$$B_{gSyn(d)}(\theta,t) = \sum_{v} B_{gSynD(v)} \cos[v(\theta - \omega t)] \tag{25}$$

where $B_{gSynD(v)} = (\psi_{m1} + L_{m(d)} i_d) / k_{B2\psi}$ for ($v = 1$) and…

$$B_{gSynD(v)} = \left[\frac{\psi_{m1}}{\sin(\alpha_{pa}/2)} - \frac{4L_{m(d)} i_d}{\pi k_{ad(d)}} \frac{\Re_m}{\Re_m + \Re_g} \frac{\sin(\alpha_{pa}/2)}{(\alpha_{pa}/2)}\right] \times \frac{1}{k_{B2\psi}} \sum_{v} \frac{\sin(v\alpha_{pa}/2)}{v}$$

for ($v \neq 1$)

$$B_{gSyn(q)}(\theta,t) = \sum_{v} B_{gSynQ(v)} \sin[v(\theta - \omega t)] \tag{26}$$

where $B_{gSynQ(v)} = (L_{m(q)} i_q / k_{B2\psi})$ for ($v = 1$) and…

$$B_{gSynQ(v)} = -\frac{8}{\pi} \frac{\mu_0 r l_{stk}}{n_p l_g} \frac{\sin[\frac{\alpha_{pa} + \alpha_{lm}}{2}] \sin(\frac{\alpha_{lm}}{2})}{(\mathrm{P}_{br} + \mathrm{P}_{g(lm)})} \frac{L_{m(q)} i_q}{k_{ad(q)}} \times \frac{1}{k_{B2\psi}} \sum_{v} \frac{\cos(v\alpha_{pa}/2) - \cos[v(\alpha_{pa}/2) + v\alpha_{lm}]}{v}$$

for ($v \neq 1$)

Results from (25) and (26) could be employed to compute the synchronous airgap flux density $B_{gSyn}(\theta,t)$ in (27) where $B_{gSynH(v)} = \sqrt{B^2_{gSynD(v)} + B^2_{gSynQ(v)}}$ and γ_v is the relevant harmonic angle computing from dq-axis synchronous harmonic magnitudes.

$$B_{gSyn}(\theta,t) = \sum_{v} B_{gSynH(v)} \cos[v(\theta - \omega t) - \gamma_v] \tag{27}$$

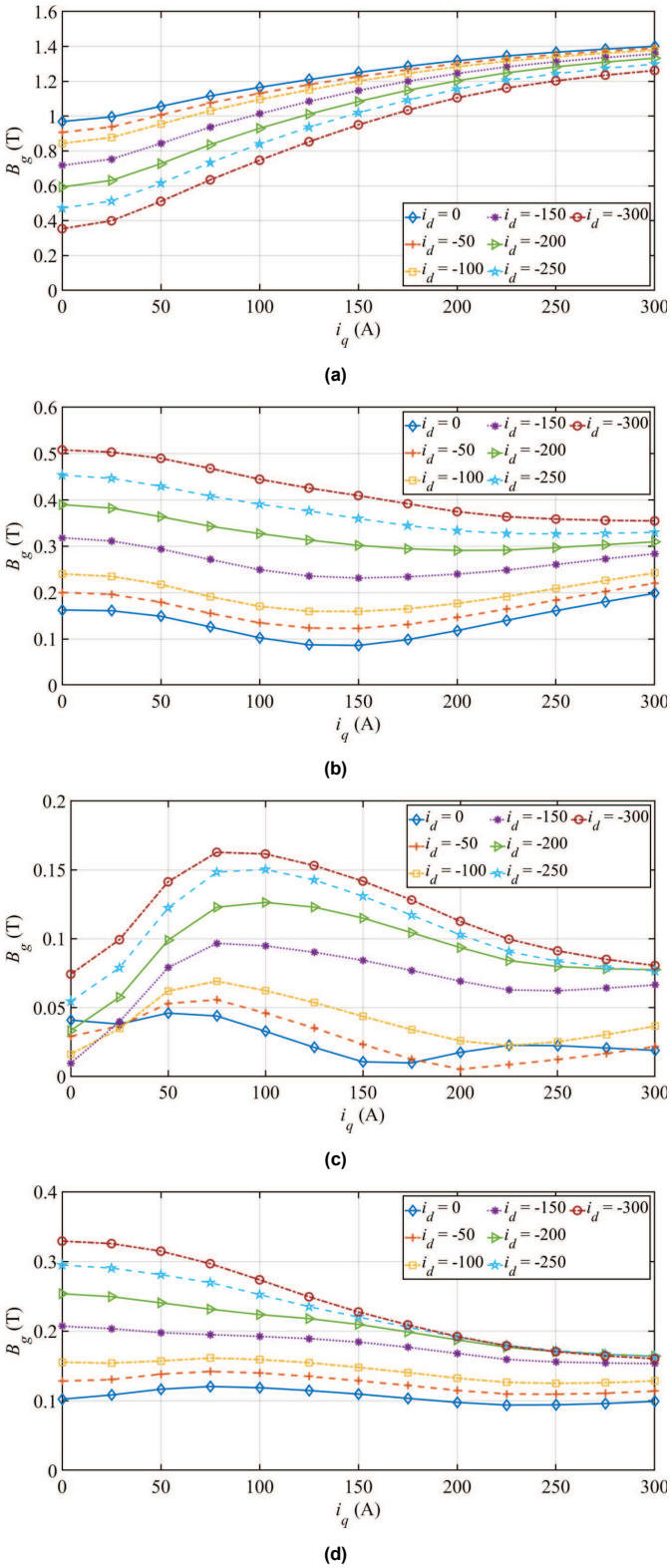

FIG. 5. Total airgap flux density considering all harmonics obtained from FEA. (a) Fundamental harmonic. (b) 3rd order harmonic. (c) 5th order harmonic. (d) 7th order harmonic.

The average synchronous stator tooth flux density $B_{tSyn}(t)$ could be obtained in (28) by integrating the $B_{gSyn}(\theta,t)$ over a

stator slot-pitch [20], [21], [26] where $\alpha_t = 2\pi n_p/n_{slt}$ is the tooth pitch angle.

$$B_{tSyn}(t) = \frac{\pi D_{is}}{t_{wd} n_{slt}} \sum_{v} B_{gSyn(v)} \frac{\sin(v\alpha_t/2)}{(v\alpha_t/2)} \cos(v\omega t - \gamma_v) = \sum_{v} B_{tSyn(v)} \cos(v\omega t - \gamma_v) \quad (28)$$

On the other hand, the synchronous flux density in the stator yoke $B_{ySyn}(t)$ could be considered as constant over the radial direction and therefore its average value could be obtained in (29) by integrating the $B_{gSyn}(\theta,t)$ over a full period [20], [21], [26].

$$B_{ySyn}(t) = \frac{D_{is}}{2 y_{wd} n_p} \sum_{v} B_{gSyn(v)} \frac{\sin(v\pi/2)}{v} \cos(v\omega t - \gamma_v) = \sum_{v} B_{ySyn(h)} \cos(v\omega t - \varphi) \quad (29)$$

For magnetic saturation analysis, magnitudes of total airgap flux density fundamental and selected high-order harmonic components obtained from FEA under full range on-load *dq*-axis currents are presented in Fig. 5. It is noted that the 3rd order harmonic magnitude is only contributed by the synchronous component and the 5th and 7th order harmonic magnitudes are mainly contributed by the synchronous components as aforementioned. It is also noted that the tested machine maximum fundamental airgap flux density is 1.25T (2.04T tooth flux density) and all the operation points higher than 1.25T in Fig. 5(a) are only for evaluating the proposed method under extremely high flux density condition. As can be seen, in the operation region with high-*d*-axis current and low-*q*-axis current, the 3rd order harmonic magnitude could be comparable and even higher than the fundamental component under some specific operation conditions, Figs. 5(a) and 5(b). In addition, the 5th and 7th order harmonic magnitudes are also considerably high, Figs. 5(c) and 5(d). This phenomenon is in good agreement with (25) where it is shown that an increase of *d*-axis current may result in an increase of the *d*-axis high-order synchronous harmonic magnitudes (v = 3,5,7…). Thus, the high-order synchronous airgap flux density components should be considered together with the fundamental component for nonlinear magnetic analysis. On the other hand, Fig. 5 also shows that for a given *d*-axis current, when the *q*-axis current increases causing the fundamental flux density to be increased and becomes significantly high compared with the high-order harmonic magnitudes, the high-order harmonic magnetics becomes reduced. This phenomenon could be explained by the increase of magnetic saturation level due to the increase of the fundamental component. Obviously, the effects of the high-order airgap flux density harmonics on the magnetic saturation may become limited if their magnitudes become lower than the fundamental component. Due to the space limitation, other harmonics are not presented in the paper but similar conclusions are also obtained.

For the simplified EMC model in Fig. 2, the fundamental component of the $B_{gSyn}(\theta,t)$ in (27) over a full space period is often employed for magnetic saturation analysis. Based on the total RMS theory [26], the equivalent total synchronous airgap flux density considering high-order synchronous airgap flux density harmonics over a full space period for magnetic saturation analysis could be derived from (27) as shown in (30) (v = 1,3,5,7…). As can be seen, the high-order harmonic airgap flux densities are significantly contributed to the $B_{gSyn\Sigma}$ when their magnitudes are comparable or higher than the fundamental component and become limited when their magnitudes are significantly lower than the fundamental value.

$$B_{gSyn\Sigma} = \sqrt{\sum_{v} B^2_{gSynH(v)}} \quad (30)$$

In electric machines, the magnetic saturation level in the iron teeth is often higher than the iron yoke [26], [27]. Thus, using (28), the equivalent tooth flux density $B_{tSyn\Sigma}$ for magnetic saturation analysis could be defined in (31).

$$B_{tSyn\Sigma} = \frac{\pi D_{is}}{t_{wd} n_{slt}} B_{gSyn\Sigma} \quad (31)$$

B. CONSIDERATION OF MAGNETIC NONLINEARITY ON MACHINE PARAMETER DETERMINATION

For magnetic nonlinearity consideration, a process loop using *BH* curve of the selected material (M270-35A) [28], Fig. 6, to determine the relevant $\mu_{rFe}(i_d,i_q)$ from the obtained tooth flux density $B_{tSyn\Sigma}$ (31) under different *dq*-axis currents applied is proposed in Fig. 7. As can be seen, the process loop consists of two iterative loops, an outer loop for processing different sets of *dq*-axis currents and an inner loop for determining the relevant $\mu_{rFe}(i_d,i_q)$ from the obtained $B_{tSyn\Sigma}$ associated with one set of *dq*-axis currents. It is noted that when the tooth flux density under the process loop is higher than 1.85T, Fig. 6, the relevant μ_{rFe} becomes significantly low. This may lead the inner loop to an unsatisfactory equilibrium point. In practice, electric machine is often not designed for continuous operation with a flux level higher than 1.9T (only for short-period overload operation, e.g. a maximum peak tooth flux density as 2.04T for the tested IPM machine) to avoid low efficiency performance [26], [27]. Therefore, iterative deviation at tooth flux level higher than 1.9T [*H* is higher than around 30(kA/m), see Fig.6] may not significantly affect the proposed method.

At first, an initial value (7900 for M270-35A) for the no-load μ_{rFe_Int} (i_d = 0 and i_q = 0) is selected to compute the initial no-load parameters using (9) and (21). Then, the obtained initial parameters are utilized together with μ_{rFe_Int} to calculate the initial tooth flux density $B_{tSyn\Sigma}$ (0) at step(0) associated with the relevant *dq*-axis current set using (31). Based on the *BH* curve, the revised initial $\mu_{rFe}(0)$ could be derived. These values are utilized as the inputs for an inner iterative loop terminating at the step (k+1) when the absolute difference between $B_{tSyn\Sigma}(k)$ and $B_{tSyn\Sigma}(k+1)$ is below a desired error ε. To maintain a smooth iterative process, a damping factor k_1=0.8 is employed [7]. For avoiding infinite loop issue, a maximum step k_{max} is utilized as a break condition. The results obtained from the inner loop for the given set *dq*-axis currents will be stored in the

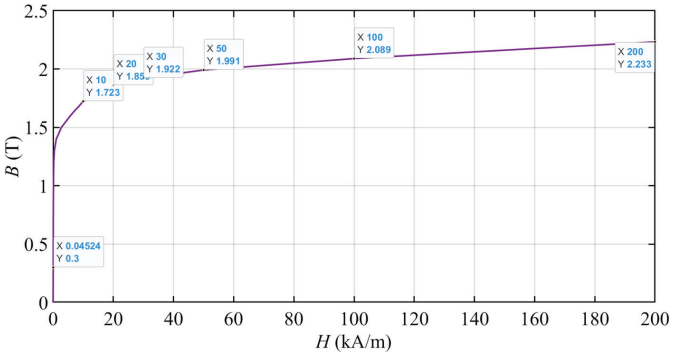

FIG. 6. ***BH*** **curve of employed magnetic material (M270-35A) [28].**

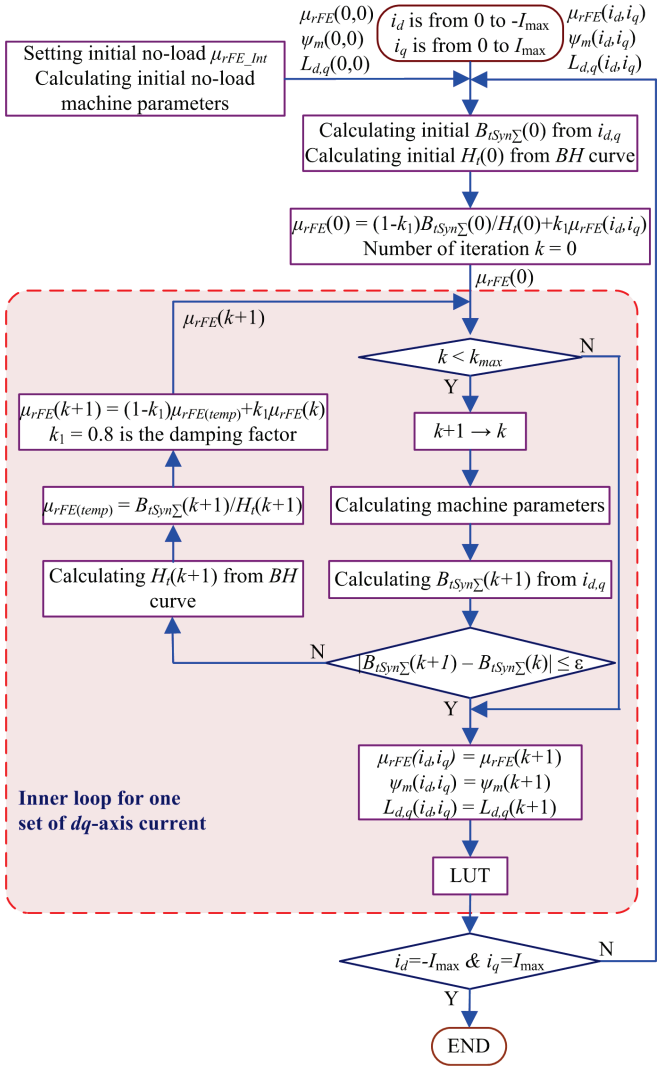

FIG. 7. **Process loop for proposed rapid evaluation methodology.**

look-up table (LUT) and then employed as the inputs for the next outer loop with a new set of *dq*-axis currents.

The obtained synchronous airgap flux densities under the proposed method in (27) using the process loop in Fig. 7 are presented in Figs. 8. It is noted that the conversion factor from the fundamental airgap flux density to the tooth flux density is computed as 1.6301 using (28). Comparison

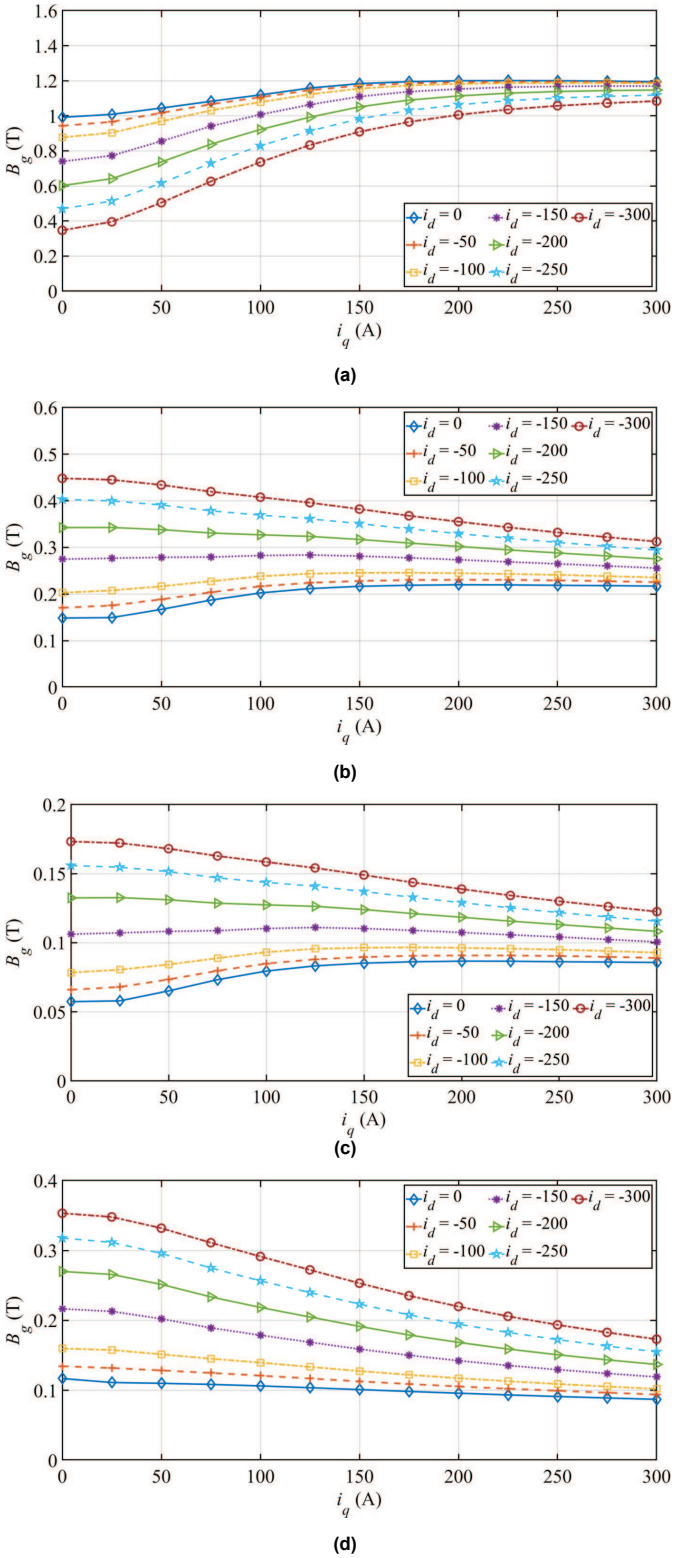

FIG. 8. **Synchronous airgap flux density obtained from proposed method [see (27)]. (a) Fundamental harmonic. (b) 3rd order harmonic. (c) 5th order harmonic. (d) 7th order harmonic.**

between Figs. 8(a) and 5(a) presents a good agreement between FEA and the proposed method for a fundamental airgap flux density up to 1.1T (1.793T tooth flux density

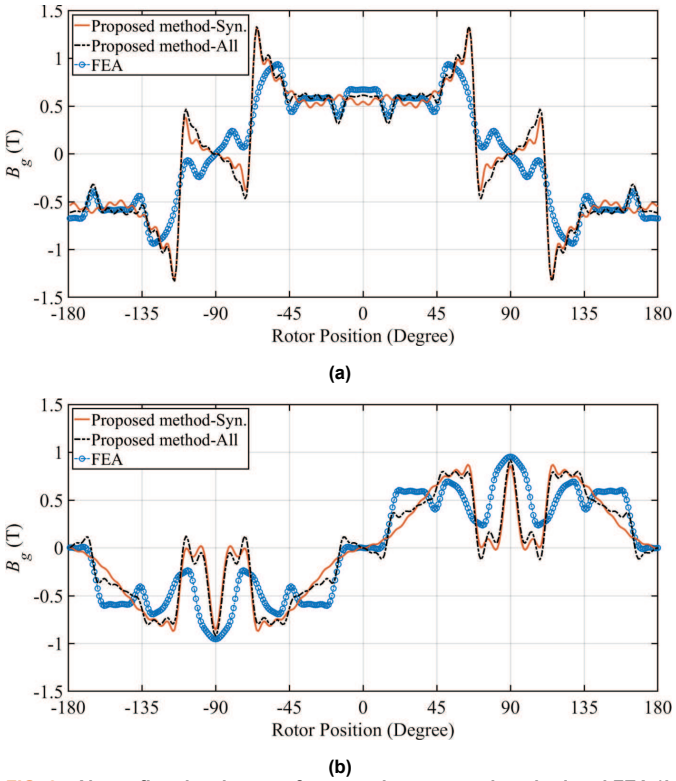

FIG. 9. Airgap flux density waveforms under proposed method and FEA (i_d = -100A, i_q = 100A). (a) *D*-axis flux density. (b) *Q*-axis flux density.

using the conversion factor). For the airgap flux density higher than 1.1T, despite the aforementioned inner loop deviation issue associated with high magnetic saturation, Fig. 6, an acceptable agreement with a difference up to 10-15% could still be obtained for the proposed method at i_q = 300A, i_d is from -300A to 0A [1.25T to 1.4T airgap flux density, 2.04T to 2.28T tooth flux density using the conversion factor, H is around from 100(kA/m) to 200(kA/m) under FEA, see Figs. 5(a) and 6]. It is noted that the tested machine maximum fundamental airgap flux density is 1.25T (2.04T tooth flux density) and all the operation points higher than 1.25T presented in Fig. 5(a) are only for evaluating the proposed method under extremely high flux density condition. Fig. 8 also shows a considerable match for the high-order synchronous harmonics under the proposed method compared with relevant FEA results, Fig. 5. It is also noted that the obtained good match for the fundamental component highly demonstrates the necessary of considering the high-order synchronous harmonics for nonlinear magnetic analysis. In the next section, highly deviated parameters obtained from the process loop without considering the high-order synchronous harmonics will be presented [see Figs. 11(a), 12(a), and 13(a)]. The obtained high-order synchronous flux density harmonics are also essential for iron loss determination [20], [21]. To further demonstrate the proposed method, airgap flux density waveforms of the tested machine under loaded condition (i_d = -100A, i_q = 100A, tooth flux density as 1.8T) considering all harmonics [see (8), (17), and (20)], only synchronous harmonics [see (25), (26)], and FEA are presented in Fig. 9 where acceptable matches between the proposed method and FEA could be observed.

V. LOSS DETERMINATION

A. IRON LOSS DETERMINATION CONSIDERING SYNCHRONOUS HARMONIC EDDY-CURRENT LOSS

Based on the flux densities obtained from the process loop, Fig. 8, the machine stator iron loss P_{lossFe} [1], [26] could be computed in (32) where P_{FeHys}, P_{FeEd}, and P_{FeEx} is respectively the hysteresis component, the eddy current component considering high-order synchronous flux density harmonics (v = 1,3,5,7…) [see (28), (29)] [20], [21], and the exceeding component; V_{tFe} and V_{yFe} is respectively the stator tooth and stator yoke volume; f is the operating frequency; k_{hys}, k_{ed}, and k_{ex} is respectively the relevant hysteresis, eddy current, and exceeding coefficients extracted from the manufacturer datasheet [28]. As contribution of rotor iron loss in total IPM machine iron loss is quite limited (10 to 15%) [18], an assumption for 10% contribution of rotor iron loss in total machine iron loss is utilized.

$$P_{FeHys} = k_{hys} f (V_{tFe} B_{tSyn(1)}^2 + V_{yFe} B_{ySyn(1)}^2) \quad (32.a)$$

$$P_{FeEd} = k_{ed} f^2 (V_{tFe} \sum_v v^2 B_{tSyn(v)}^2 + V_{yFe} \sum_v v^2 B_{ySyn(v)}^2) \quad (32.b)$$

$$P_{FeEx} = k_{ex} f^{1.5} (V_{tFe} B_{tSyn(1)}^{1.5} + V_{tFe} B_{ySyn(1)}^{1.5}) \quad (32.c)$$

Iron loss of the tested machine under different *dq*-axis currents at 5000rpm using the proposed method and FEA is presented in Fig. 10(a) and 10(b). As can be seen, in comparison with the FEA, an acceptable iron loss for the tested IPM machine up to a fundamental airgap flux density level around 1.1T (1.793T tooth flux density) [see Fig. 5(a)] could be achieved. For flux density higher than this level, due to the inner loop deviation associated with extreme magnetic saturation (see Fig. 6), a difference up to 20% iron loss could be observed at i_q = 300A and i_d is from -300A to 0A [1.25T to 1.4T airgap flux density, 2.04T to 2.28T tooth flux density using the conversion factor, H is around from 100(kA/m) to 200(kA/m) under FEA, see Figs. 5(a) and 6]. It is noted that since electric machine is often not designed for continuous operation with a flux level higher than 1.9T (only for short-period overload operation, e.g. a maximum peak tooth flux density as 2.04T for the tested IPM machine) to avoid low efficiency performance [26], [27], up to 20% iron loss deviation at tooth flux level from 2.04T to 2.28T may not significantly affect the proposed method. Similar conclusions could also be obtained for the tested IPM machine under other speed levels up to the maximum speed (15krpm).

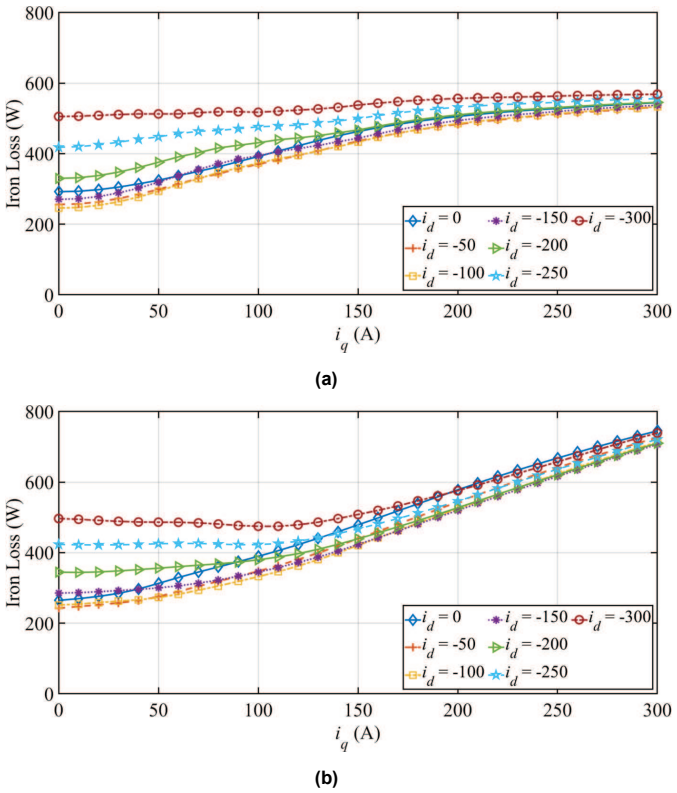

FIG. 10. **Iron loss under proposed method and FEA for tested machine at 5krpm. (a) Proposed method. (b) FEA.**

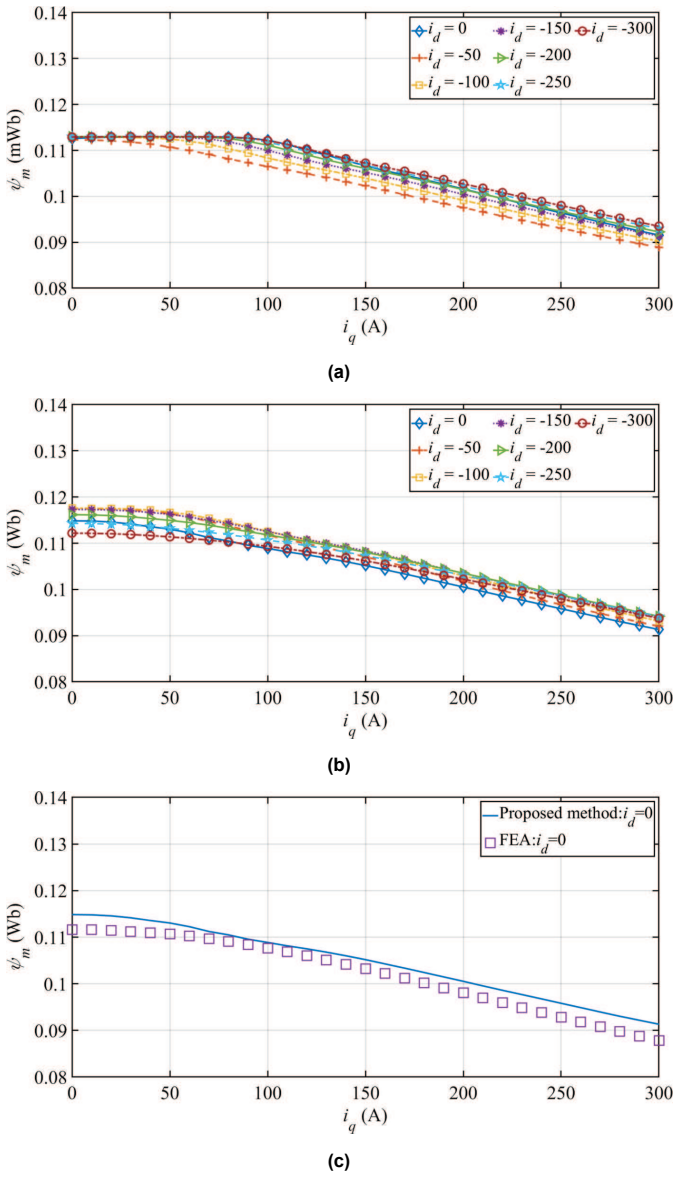

FIG. 11. **PM flux linkage. (a) Process loop (Fig. 7) without considering synchronous flux density harmonics. (b) Proposed method. (c) FEA.**

B. COPPER LOSS DETERMINATION CONSIDERING TEMPERATURE VARIATION AND AC LOSS

In [18], calculation of stator winding resistance considering temperature variation and AC loss, $R_{s(T,f)}$, was presented as shown in (33) where r_{tc} is the copper resistivity temperature coefficient; ΔT is the delta temperature; T_0 is the reference temperature; T is the conductor temperature; $\rho_{Cu(T0)}$ is the copper resistivity at T_0; $k_{AC(T,f)}$ is the ratio between the DC and AC resistance. Since the machine strand diameter, Table I, is selected to mitigate the switching frequency at 12kHz, d_{stnd} is also smaller than the skin-depth $\delta_{(T,f)}$ associated with the operating fundamental frequency (1kHz) at the maximum speed (15krpm). Under this specific condition, $k_{AC(T,f)}$ could be simplified as (34) [25]. Results obtained from (33) could be employed to compute the copper loss, P_{lossCu}, at a given torque-speed operation point using the optimum operating dq-axis currents [i.e. maximum torque per ampere (MTPA) control at low-speed region and FW control at high-speed region] [18].

$$R_{s(T,f)} = (1 + r_{tc}\Delta T / \rho_{Cu(T0)})R_{s(T0)}k_{AC(T,f)} \quad (33)$$

$$k_{AC(T,f)} \approx 1 + (1/9)(s_{dpt} / \delta_{(T,f)})^2 (d_{stnd} / \delta_{(T,f)})^2 \quad (34)$$

VI. VALIDATION OF PROPOSED RAPID EVALUATION TECHNIQUE

The proposed technique is validated with the high-speed high-power (15kRPM, 120kW) IPM traction machine presented in Fig. 1 and Table I using FEA results as a benchmark. To obtain a high-accuracy result, the FEA model is solved with 0.5 electrical degree step for different dq-axis currents from 0 to I_{max} (negative i_d) with 10A step. In terms of the computation time, the developed FEA model has a total 15499 elements requiring a couple of days to obtain the full parameter information. In comparison, the proposed method takes only a couple of minutes to obtain the full parameter information with limited computer resource [3 minutes for a computer equipped with an i7-M4810MQ CPU, the inner loop desired error ε is selected as 1%, the maximum step k_{max} is set as 100 steps, dq-axis current is varied from 0 to I_{max} (negative i_d) with 1A step]. Therefore, the proposed model is very essential to quickly evaluate a defined machine design specification without the requirement of FEA.

The machine parameters obtained under the process loop (see Fig. 7) without and considering the high-order synchronous flux density harmonics for nonlinear magnetic

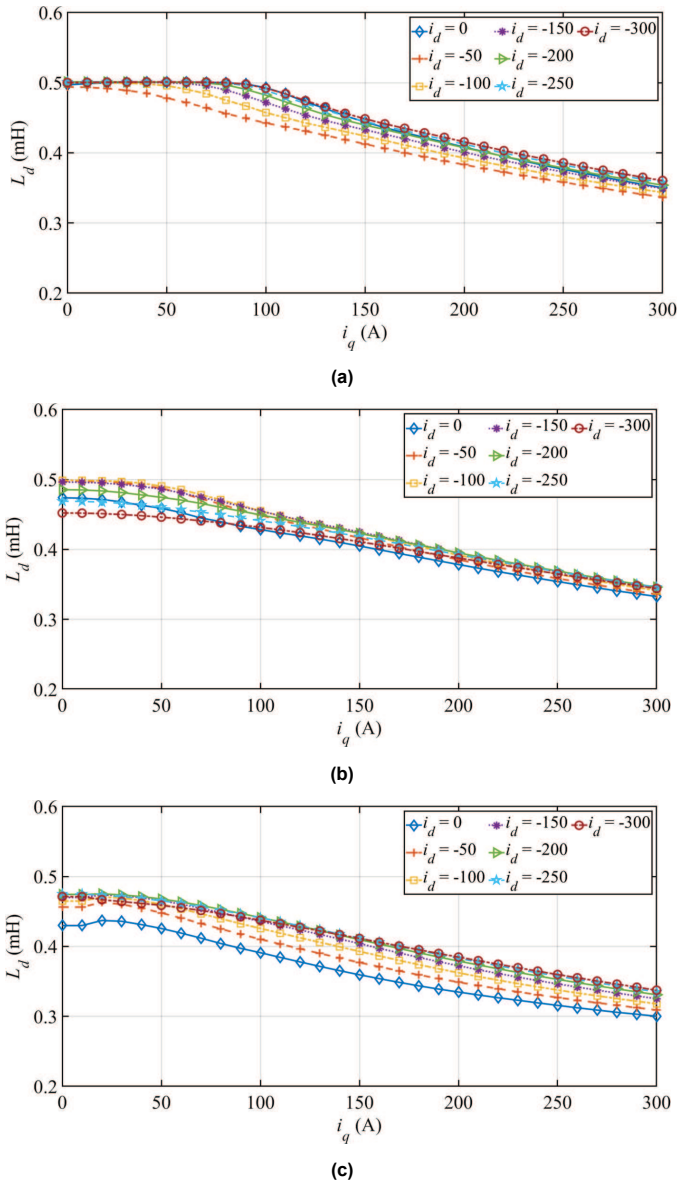

FIG. 12. *D*-axis inductances. (a) Process loop (Fig. 7) without considering synchronous flux density harmonics. (b) Proposed method. (c) FEA.

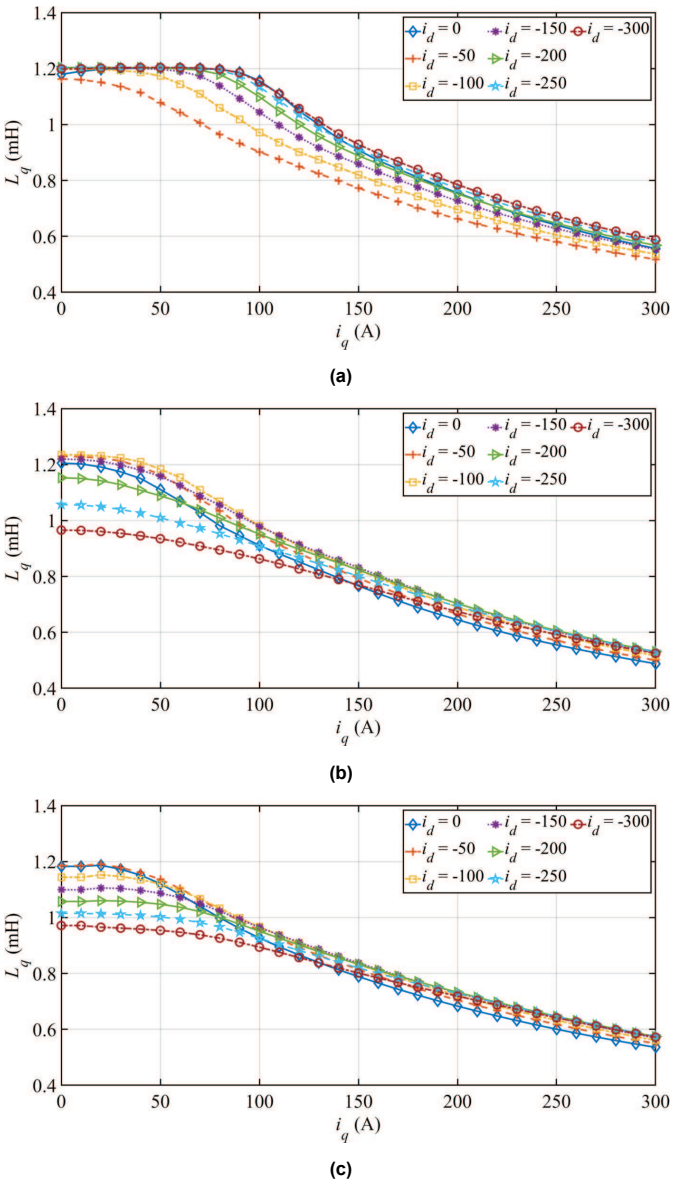

FIG. 13. *Q*-axis inductances. (a) Process loop (Fig. 7) without considering synchronous flux density harmonics. (b) Proposed method. (c) FEA.

analysis together with relevant FEA results is respectively presented in Figs. 11, 12, and 13 for the PM flux linkage and *dq*-axis inductances. As can be seen in Figs. 11(a), 12(a), and 13(a), under the high-*d*-axis current and low-*q*-axis current operation region, in comparison with FEA results, high deviation on parameters obtained under the process loop without considering the synchronous flux density harmonics for nonlinear magnetic analysis could be observed. On the other hand, Fig. 11(c) shows a good agreement between FEA and the proposed method for the PM flux linkage with i_d =0 and i_q is from 0 to 300A. It is noted that the PM flux linkage under the proposed method is varied as a function of both *dq*-axis currents [see Fig. 11(b)] whereas it is only assumed as a function of *q*-axis current with i_d = 0 [see Fig. 11(c)] under FEA and the variation of the PM flux linkage due to *d*-axis current will be introduced into the *d*-axis inductance [see Fig. 12(c)]. However, an acceptable agreement could still be obtained for the *d*-axis inductance under the proposed method [see Fig. 12(b)] compared with FEA. In addition, comparison between Figs. 13(b) and 13(c) shows that a significant agreement in the *q*-axis inductance could be achieved for the proposed method. It is noted that Figs. 13(b) and 13(c) highly presents the magnetic saturation effects on the *q*-axis inductance under high-*d*-axis current and low-*q*-axis current operation. To further demonstrate the proposed method, the differences in the *dq*-axis inductances compared with FEA are shown in Fig. 14. As can be seen, the proposed method could obtain *dq*-axis inductances with up to 10% difference under extreme magnetic saturation and deep FW operation. It is noted that the tested machine maximum fundamental airgap flux density is 1.25T (2.04T tooth flux density) and

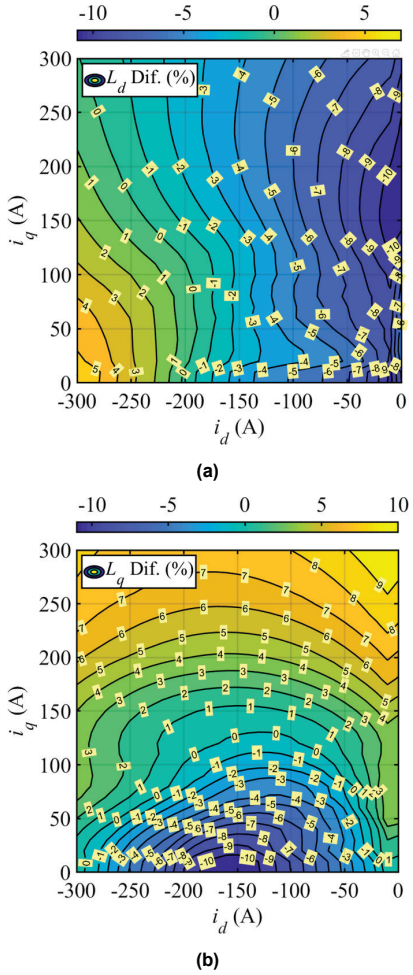

FIG. 14. Difference between proposed method and FEA results. (a) *D*-axis inductance. (b) *Q*-axis inductance.

all the operation points higher than 1.25T [see Fig. 5(a)] are only for evaluating the proposed method under extremely high flux density operation [i.e. H is around from 100(kA/m) to 200(kA/m) under FEA, see Figs. 5(a) and 6].

Using the obtained parameters, the copper loss for the full torque-speed operation map [1], [18] is presented in Fig. 15(a) with the FEA result is shown in Fig. 15(b). It is noted that determination of the optimum *dq*-axis currents from the obtained parameters for torque-speed operation map were well presented in [1], [2] and [18] and are not discussed in the paper to avoid duplication. As can be seen, in the low-speed low-torque operation region, copper loss under the proposed method is significantly matched with the FEA. However, in the low-speed high-torque extreme saturation region (175-225Nm), a higher than expected copper loss could be observed, Fig. 15(a). In addition, in the high speed operation region (12.5-15krpm), a higher than expected copper loss could also be noticed. On the other hand, iron loss over torque-speed operation map for the tested machine is shown in Fig. 16(a) and relevant FEA results is depicted in Fig. 16(b). As can be seen, in the high speed operation region (12.5-15krpm), a higher than expected iron loss compared with the FEA could be

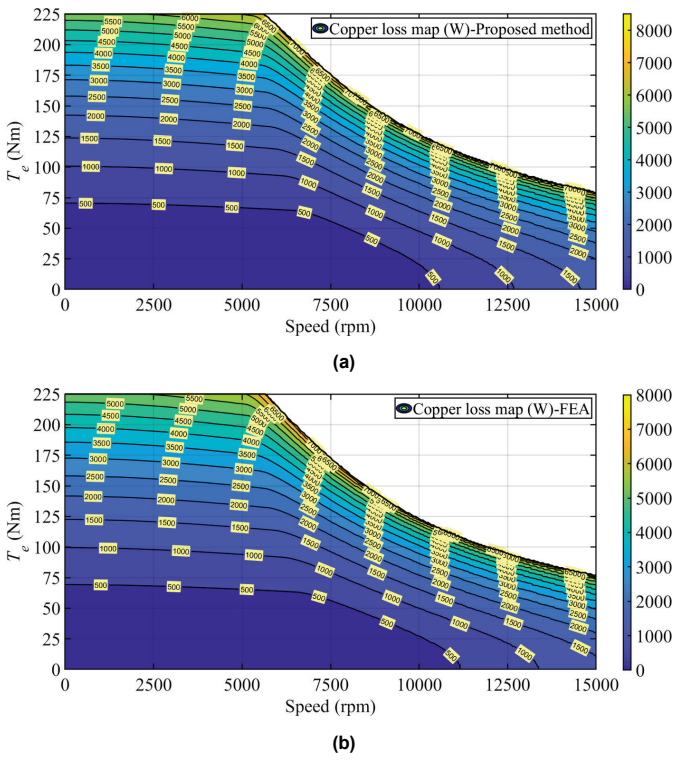

FIG. 15. Copper loss map (W). (a) Proposed method. (b) FEA.

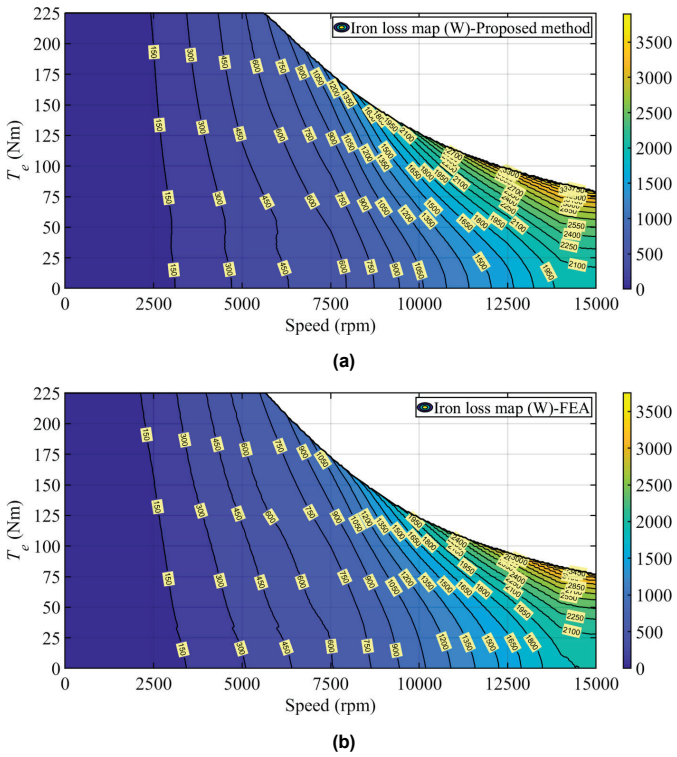

FIG. 16. Iron loss map (W). (a) Proposed method. (b) FEA.

observed. However, since the tested IPM machine is under high power operation mode in the extreme saturation and deep FW operation regions, loss calculation deviation in these operation regions may not significantly affect the machine efficiency determination. Based on the obtained

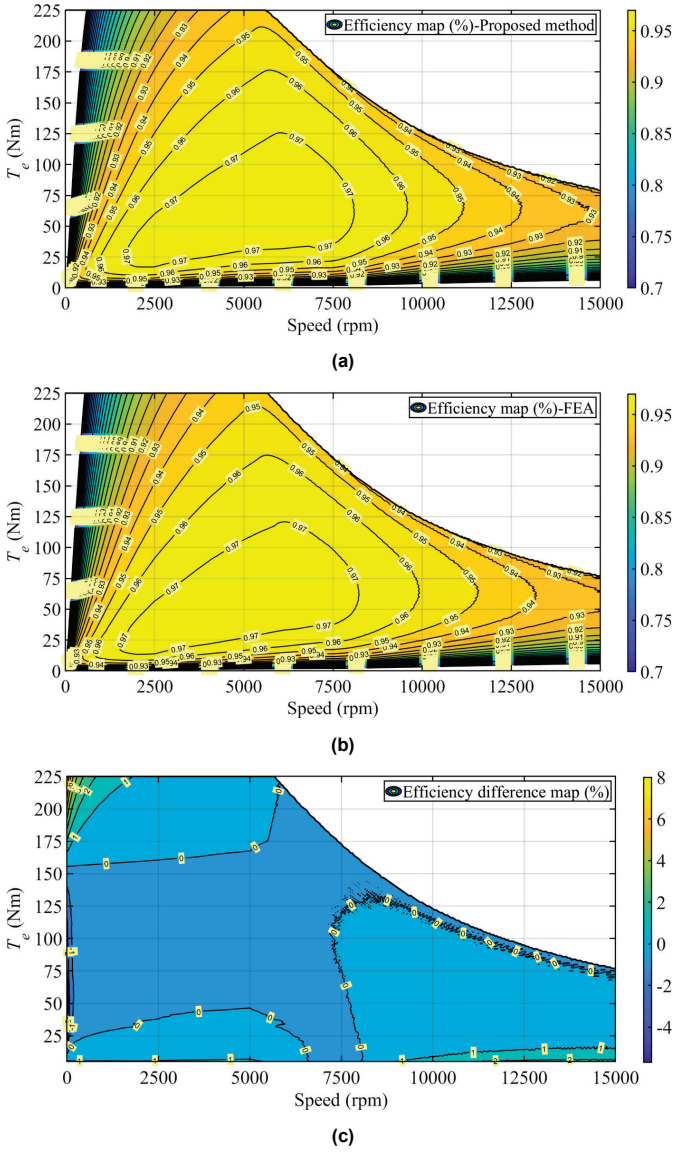

FIG. 17. Efficiency map. (a) Proposed method. (b) FEA. (c) Efficiency difference (%).

loss maps, relevant machine efficiency map is presented in Fig. 17(a). In comparison with the FEA result [see Fig. 17(b)], a very similar efficiency for the tested IPM machine could be achieved for the proposed method, with up to 1% efficiency difference within the main torque-speed operation region [see Fig. 17(c)]. Moreover, the efficiency measurement of the tested IPM machine could be found in [29] where a good match between the measurement and the proposed rapid evaluation method could be observed.

VII. CONCLUSION

In the paper, a reasonably accurate and fast analytical evaluation technique for rapid parameter and efficiency determination of IPM traction machines considering magnetic nonlinearity under full-range on-load *dq*-axis currents is presented. The main contributions of the paper are highlighted as follows

1. A simplified analytical model with sufficient accuracy for rapid evaluation a given IPM machine design specification.
2. The necessary of considering high-order synchronous flux density harmonics for nonlinear magnetic analysis.

Under the proposed technique, sufficiently accurate parameters (up to 10% difference under extreme-saturation and deep-FW operation conditions) and efficiency (up to 1% efficiency difference within the main torque-speed operation region) for the tested IPM machine compared with the FEA could be produced within minutes. Thus, the proposed technique is very essential to quickly validate a defined IPM machine design specification at the preliminary design stage without the requirement of the FEA.

It is noted that the simplified analytical model in the paper is developed for a particular IPM machine configuration with single-magnet layer rotor. Since the EMC model and winding function for IPM machine with multi-magnet layer rotor could be obtained by modifying the single magnet layer rotor EMC model [6]-[8], the proposed method is equally applicable to IPM machines with multi-magnet layer rotor.

Future work will include consideration of the simplified analytical model for IPM traction machines with FSCW configuration. Since winding function methodology was proven to be suitable for analyzing both IPM machines with distributed-winding configuration and FSCW configuration [10], the proposed method employing a simplified EMC model together with the winding function could be modified for FSCW IPM traction machine by considering the subharmonic spatial airgap flux components [30], [31] for magnetic saturation analysis and loss determination.

ACKNOWLEDGMENT

The author would like to thank the anonymous reviewers for their valuable comments and suggestions that greatly contributed to improve the quality of this paper.

REFERENCES

[1] K. D. Hoang and K. Atallah, “A rapid concept development technique for electric vehicle power trains,” *in Proc. IEEE Int. Conf. Connected Vehicles and Export (ICCVE) 2014*, Vienna, Austria, Nov. 3-7, 2014, pp. 191-198.

[2] K. D. Hoang, J. Wang, M. Cyriacks, A. Melkonyan and K. Kriegel, "Feed-forward torque control of interior permanent magnet brushless AC drive for traction applications," *in Proc. Int. Conf. Electric Mach. Drives IEMDC 2013*, pp. 152-159, 2013.

[3] V. B. Honsinger, "The fields and parameters of interior type AC permanent magnet machines," *IEEE Trans. Power Apparatus and Systems*, vol. PAS-101, no. 4, pp. 867-876, April 1982.

[4] J. F. Gieras, E. Santini, and M. Wing, “Calculation of synchronous reactances of small permanent-magnet alternating-current motors: Comparison of analytical approach and finite element method with measurement,” *IEEE Trans. Magn.*, vol. 34, no. 5, pp. 3712–3720, Sep. 1998.

[5] C. C. Hwang and Y. H. Cho, "Effects of leakage flux on magnetic fields of interior permanent magnet synchronous motors," *IEEE Trans. Magn.*, vol. 37, no. 4, pp. 3021-3024, Jul 2001.

[6] E. C. Lovelace, T. M. Jahns, and J. H. Lang, "A saturating lumped-parameter model for an interior PM synchronous machine," *IEEE Trans. Ind. Appl.*, vol. 38, no. 3, pp. 645-650, May/June 2002.

[7] S. Han, T. M. Jahns, and W. L. Soong, "A magnetic circuit model for an IPM synchronous machine incorporating moving airgap and cross-coupled saturation effects", *Proc. Int. Conf. Electrical Mach. and Drives IEMDC 2007*, pp. 21-26, 2007-May-35.
[8] L. Zhu, S. Z. Jiang, Z. Q. Zhu, and C. C. Chan, "Analytical modeling of open-circuit air-gap field distributions in multisegment and multilayer interior permanent-magnet machines," *IEEE Trans. Magn.*, vol. 45, no. 8, pp. 3121-3130, Aug. 2009.
[9] Q. Li, T. Fan, and X. Wen, "Armature-reaction magnetic field analysis for interior permanent magnet motor based on winding function theory," *IEEE Trans. Magn.*, vol. 49, no. 3, pp. 1193–1201, Mar. 2013.
[10] H. Chen, D. Li, R. Qu, Z. Zhu, and J. Li, "An improved analytical model for inductance calculation of interior permanent magnet machines," *IEEE Trans. Mag.*, vol. 50, no. 6, pp. 1-8, June 2014.
[11] P. Liang, Y. Pei, F. Chai, Y. Bi and S. Cheng, "An improved method for armature-reaction magnetic field calculation of interior permanent magnet motors," *IEEE Trans. Magn.*, vol. 52, no. 7, pp. 1-4, Jul. 2016.
[12] K. Lee, J. Lee, and H. Lee, "Inductance calculation of flux concentrating permanent magnet motor through nonlinear magnetic equivalent circuit," *IEEE Trans. Magn.*, vol. 51, no. 11, pp. 1-4, Nov. 2015.
[13] L. Guo, C. Xia, H. Wang, Z. Wang, and T. Shi, "Improved equivalent magnetic network modeling for analyzing working points of PMs in interior permanent magnet machine", *Journal of Magnetism and Magnetic Materials*, volume 454, 2018, pp. 39-50.
[14] Z. Li, X. Huang, L. Wu, T. Long, B. Shi, and H. Zhang, "Open-circuit field prediction of interior permanent-magnet motor using hybrid field model accounting for saturation," *IEEE Trans. Magn.*, vol. 55, no. 7, pp. 1-7, July 2019.
[15] L. Xu, C. Zhang, X. Zhu, M. Lin and S. Zheng, "Indirect analytical modeling and analysis of V-shaped interior PM synchronous machine," *IEEE Access*, vol. 7, pp. 173786-173795, 2019.
[16] M. M. Ghahfarokhi, E. Amiri, S. T. Boroujeni and A. D. Aliabad, "On-load analytical modeling of slotted interior magnet synchronous machines using magnetic islands method," *IEEE Access*, vol. 8, pp. 95360-95367, 2020.
[17] S. Wu, T. Shi, L. Guo, H. Wang and C. Xia, "Accurate analytical method for magnetic field calculation of interior PM motors," *IEEE Trans. Energy Conversion (early access)*, doi: 10.1109/TEC.2020.3000753.
[18] K. D. Hoang, K. Atallah, P. Lazari, J. Birchall, and S. Calverley, "Thermal analysis and control development of interior PM traction machines," *in Proc IEEE IECON'2019,* Lisbon, Portugal, pp. 1399-1404, 14 -17 Oct. 2019.
[19] S. H. Han, W. L. Soong, T. M. Jahns, M. K. Güven, and M. S. Illindala, "Reducing harmonic eddy-current losses in the stator teeth of interior permanent magnet synchronous machines during flux weakening," *IEEE Trans. Energy Convers.*, vol. 25, no. 2, pp. 441-449, June 2010.
[20] C. Tang, W. L. Soong, T. M. Jahns, and N. Ertugrul, "Analysis of ion loss in interior PM machines with distributed windings under deep field weakening," *IEEE Trans. Ind. Appl.*, vol. 51, no. 5, pp. 3761-3772, Sept./Oct. 2015.
[21] Q. Li, T. Fan, and X. Wen, "Characterization of iron loss for integral-slot interior permanent magnet synchronous machine during flux weakening," *IEEE Trans. Magn.*, vol. 53, no. 5, pp. 1-8, May 2017.
[22] A. Balamurali, A. Kundu, W. Clandfield, and N. C. Kar, "Non–invasive parameter and loss determination in PMSM considering the effects of saturation, cross–saturation, time harmonics and temperature variations," *IEEE Trans. Magn. (early access),* doi: 10.1109/TMAG.2020.3019459.
[23] K. D. Hoang and H. Aorith, "Online control of IPMSM drives for traction applications considering machine parameter and inverter nonlinearities," *IEEE Trans. Transportation Electrification*, vol. 1, no. 4, pp. 312-325, Dec. 2015.
[24] K. D. Hoang and K. Atallah, "Rapid sizing concept of interior permanent magnet machine for traction applications," *The Journal of Engineering*, vol. 2019, no. 17, pp. 3956-3961, June 2019.
[25] D. Hanselma. *Brushless motors: Magnetic design, performance, and control*. E-Man Press LLC, 2012.
[26] T. A. Lipo. Introduction to AC machine design. IEEE-Willey, 2017.
[27] T. A. Lipo. Analysis of synchronous machine. CRC, 2012.
[28] https://cogent-power.com/cms-data/downloads/m270-35a_1.pdf
[29] K. D. Hoang, P. Lazari, K. Atallah, J. G. Birchall and S. D. Calverley, "Evaluation of simplified model for rapid identification and control development of IPM traction machines," *IEEE Trans. Transportation Electrification (early access)*, doi: 10.1109/TTE.2020.3023888.
[30] G. Dajaku, H. Hofmann, F. Hetemi, X. Dajaku, W. Xie, and D. Gerling, "Comparison of two different IPM traction machines with concentrated winding," *IEEE Trans. Industrial Electronics*, vol. 63, no. 7, pp. 4137-4149, July 2016.
[31] H. Gurleyen and E. Mese, "A nonlinear *q*-axis inductance modeling of a 12-slot 10-pole IPM using approximate analytical methods," *IEEE Trans. Energy Conversion*, vol. 35, no. 2, pp. 621-630, June 2020.

Khoa Dang Hoang (S'10-M'12-SM'19) received the B.Eng. and M.Sc.(Eng.) degrees from Ho Chi Minh City University of Technology (HCMUT), Ho Chi Minh City, Vietnam, in 2002 and 2005, respectively, and the Ph.D. degree from the University of Sheffield, Sheffield, United Kingdom, in 2011, all in electrical and electronics engineering.

From 2011 to 2019, he was a Research Associate in the Department of Electronic and Electrical Engineering, University of Sheffield, UK, where he is currently a Research and Development Engineer. His key research interests include power conversion, advanced control techniques for electrical drives, and analysis and design of electrical machines.